

Crack growth modeling and simulation of a peridynamic fatigue model based on numerical and analytical solution approaches

D.J. Bang¹, A. Ince^{1*}, E. Oterkus², S. Oterkus²

¹Department of Mechanical, Industrial & Aerospace Engineering, Concordia University,

²Department of Naval Architecture and Marine Engineering, University of Strathclyde

*Corresponding author: Phone: + 1 (514) 848 2424, e-mail: ayhan.ince@concordia.ca

Abstract:

Fatigue crack growth assessment of 2024-T3 aluminum alloy is carried out on the basis of a recently developed peridynamic fatigue model. The governing remaining-life equation of the peridynamic fatigue model has been solved by two different approaches i.e. numerical and analytical approaches to perform fatigue-crack growth simulations for 2024-T3 aluminum specimen with a pre-existing crack. Remaining-life parameters of the numerical and analytical solution approaches are determined by calibrating with the experimental crack growth data. Fatigue crack growth predictions, and associated material deformation of the specimen under various loading conditions are simulated by the two approaches. Predicted results show that the numerical approach has shortcomings in accurate predictions of crack growth rates for the application of different loading conditions, while the analytical approach can be applied for a wide range of loading conditions with good prediction accuracy and stable simulations of the material deformation with a growing crack. Furthermore, it is found that the computational time of the analytical approach is considerably shorter in comparison with the numerical approach.

Keywords: peridynamic fatigue model; remaining-life equation; pre-existing cracks; crack growth rate

Nomenclature

FEM	finite element method	\hat{S}_{core}	dimensionless parameter
XFEM	extended finite element method	S_{max}	maximum applied stress-level
PD	peridynamics	R	stress ratio
$\rho_{(k)}$	mass density	λ	remaining life
$V_{(j)}$	incremental volume of the material point	N	loading cycle
$\mathbf{b}_{(k)}$	external body force density	N_1	loading cycle required for crack nucleation
$\mathbf{x}_{(k)}$	position vector of material point k	A'	arbitrary value
$\mathbf{x}_{(j)}$	position vector of material point j	A_1, m_1	remaining parameters for crack nucleation phase
$\mathbf{u}_{(k)}$	displacement vector at material point $\mathbf{x}_{(k)}$	A_2, m_2	remaining parameters for crack propagation phase
$\mathbf{u}_{(j)}$	displacement vector at material point $\mathbf{x}_{(j)}$	K	stress intensity factor
$\xi_{(k)(j)}$	initial relative position vector	K_{max}	maximum stress intensity factor
$\eta_{(k)(j)}$	relative displacement vector	K_{min}	minimum stress intensity factor
δ	horizon size	ΔK	stress intensity factor range
$\mathbf{s}_{(k)(j)}$	stretch between the material points $\mathbf{x}_{(k)}$ and $\mathbf{x}_{(j)}$	$\frac{da}{dN}$	crack growth rate
$\mathbf{t}_{(k)(j)}$	force density that material point $\mathbf{x}_{(j)}$ exerts on material point $\mathbf{x}_{(k)}$	Y	geometrical correction factor
$\mathbf{t}_{(j)(k)}$	force density that material point $\mathbf{x}_{(k)}$ exerts on material point $\mathbf{x}_{(j)}$	$\Delta\sigma$	stress range
φ	local damage	a	crack length
μ	history-dependent scalar-valued function	t	simulation time
\mathbf{s}_c	critical stretch	Δt	incremental time
$\mathbf{s}_{(k)(j)}^+$	stretch at higher extreme point	ADR	adaptive dynamic relaxation
$\mathbf{s}_{(k)(j)}^-$	stretch at lower extreme point	LEFM	linear elastic fracture mechanics
ε	cyclic bond strain	CCT	center cracked tension
ε_1	largest cyclic bond strain	w	width of specimen
ε_{core}	core cyclic bond strain	Δ	spacing between material points
S_{core}	core strain		

1. Introduction

Fatigue is the most common phenomenon of structural failure to have catastrophic effects on mechanical systems and structures. In several last decades, researchers have strived to understand fatigue damage mechanism that occurs in materials subjected to cyclic loadings. The stress and strain life methods [1-6] initially proposed by the researchers, can be defined as curve fitting-based methods using nominal and local stress and strain quantities. However, those approaches are mainly limited to estimating a number of load cycles allowed for prior to material failure rather than providing behavior of fatigue crack nucleation and propagation mechanism. The linear elastic fracture mechanics (LEFM) approach was introduced to address fatigue crack propagation [7]. It has been widely agreed that the LEFM methods can be applied to long cracks under small scale yielding conditions at the crack tip i.e. the Paris regime [7-8]. However, the LEFM-based methods lacked a mechanically systematic approach to fully address the behavior of fatigue crack growth mechanics in multiple length scales [8-9].

Finite element (FE) analysis is a powerful numerical method that can be applied to predict behavior of complex geometries and structures widely used in engineering applications. Thus, FE analysis appears to be usable numerical method for fatigue crack propagation, however its applicability is limited due to the singularity of discontinuities such as a crack tip or crack surfaces as governing equations include spatial derivatives in its formulation. As a potential solution to overcome this problem, special treatment(s) are often adapted. Remeshing method [10-14] is a widely used as one of those special treatments for modeling of fatigue crack propagation to simulate irregular crack growth paths by regenerating meshes at every time step of the numerical solution. However, this method requires mapping all existing nodal points to other points for the mesh regeneration, which could lead to inaccurate meshing conditions. Meshless methods [15-19] can efficiently handle discontinuities and simulate material deformation and crack growth behavior for complex 3D configurations. However, as for

boundary condition problems defined by partial differential equation, solutions often do not stably converge and the achieved accuracy is often found to be poor. The extended finite element method (XFEM) was introduced by Belytschko and Black [20] and Moes and his collaborators [21] to deal with cracks without modifying mesh conditions. Elements in discontinuities are reformulated by adding the enrichment function to approximate space, greatly improving the speed and accuracy of convergence. However, this method also requires additional criteria to include displacement enrichment function in the element.

Very recently, Silling et al. [22,23] introduced peridynamic (PD) theory to address discontinuities without any additional criteria for crack growth modeling. Since the PD governing equation does not include any spatial derivatives in its formulation, material deformation can be simulated including the fatigue damage by the solution of the PD governing equation. Therefore, the PD theory can be potentially applied to address any type of discontinuities e.g. a crack tip or crack surfaces. A number of PD studies have been recently introduced by researchers in the applications of mechanical failures. Askari and Xu and their coworkers [24,25] implemented a 3D EMU code to model and analyze the structural failure of aerospace composites. The authors performed failure analysis of composite panels due to the low-speed impact by using the PD code. Oterkus and Madenci [26] showed that the damage growth pattern can be predicted for pre-existing cracks by applying the PD theory to fracture analysis of composite materials. Diyaroglu et al. [27] reported applicability of the PD theory to predict the failure behavior and nonlinear transient deformation of composite structures under shock and blast type explosion induced loadings. Furthermore, Mitchell [28] proposed a PD plasticity model based on the state-based PD theory. The author suggested substantial yield criteria and derived modulus variables to perform implicit time integration. Madenci and Oterkus [29] developed the PD plasticity model based on von Mises yield criteria with isotropic hardening. The authors derived the expression of the yield function and plastic PD stretch in

terms of material parameters, force density, shear modulus and the horizon. In addition, a nonlinear PD model for large deformations has been developed [30, 31]. Silling and Bobaru [30] established a PD constitutive model for rubbery materials including cracks for one- and two- dimensional structures. Bang and Madenci [31] derived PD hyperelastic strain energy density functions for three types of equibiaxial, planar, and uniaxial loadings. Besides, by using the PD theory, the PD viscoelasticity model [32-35] and the PD viscoplasticity model [36-37] have been developed.

Later, the application of PD theory has been further expanded to areas of heat diffusion and corrosion problems [38-45]. Bobaru and Duangpanya [38] presented a transient heat transfer model for one-dimensional problem of a material body that undergoes growing cracks. Also, the authors [39] established a PD heat transfer model for a plate containing evolving insulated cracks and fiber reinforced composites for multi-dimensional problem. Diyaroglu et al. [40] proposed a heat diffusion model that can generate results using ANSYS software to increase computational efficiency. Xue et al. [41] introduced a state-based PD heat diffusion model integrated with a generalized heat conduction model that includes key variables of temperature and heat flux. Tan et al. [42] developed a PD model of functionally graded materials to simulate transient heat conduction in a plate with insulated cracks. In addition, a PD corrosion model was proposed by Jafarzadeh et al. [43] to quantitatively estimate not only the shape of the corroded microstructure, but also the depth of penetration into the corroded surface. Chen and Bobaru [44] established a PD corrosion damage model by linking the metal concentration with the damage of the PD mechanical bond. Rokkam et al. [45] suggested a PD approach to model crack propagation and corrosion damage phenomena in materials subjected to both corrosion and mechanical loading.

These various PD studies have been conducted on the basis that material damage can be modeled and simulated by applying the PD theory to the multi-length scale of crack growth

problems [46, 47]. Silling and Askari [48] introduced a PD fatigue model that includes a quasi-static solution capable of capturing real-time deformation of a material subjected fatigue loadings. The authors introduced the concept of “remaining life” to quantify the degree of accumulated damages that lead to cracks under cyclic loadings. Figure 1 schematically shows remaining life curves representing the crack nucleation and propagation phases, respectively. Each curve in Fig. 1 represents the degree of damage accumulation in the PD bond as the loading cycle increases. For the bond life of the crack nucleation phase, the remaining life decreases, eventually reaching zero. In addition, as for the bond life of the crack propagation phase [48], the remaining life of adjacent bond starts to decrease from the bond of the nucleated crack, and the bond breaks when the remaining life reaches to zero. All interacting bonds in the material experience a damage process of remaining life on the basis of crack nucleation and propagation. The PD fatigue model is based on the remaining life concept of crack nucleation and propagation damage states.

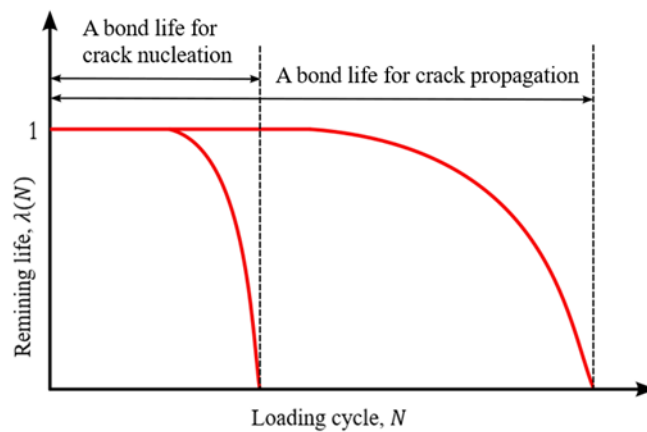


Fig. 1. Remaining life curves for crack nucleation and propagation phases.

Zhang et al. [49] demonstrated crack growth of a two-phase composite by introducing critical damage factors to validate the PD fatigue model. Freimanis and Kaewunruen [50] used PD fatigue model to present a study for rail squat crack initiation and propagation. Wang et al. [51] applied the PD fatigue model to study the effects of welding direction and hole position on the geometry of the crack path. Ma et al. [52] introduced a two-dimensional rail PD model

by considering the remaining life concept. However, these studies focused on the simulations of fatigue-crack propagation by using the remaining-life equation without demonstrating the process of determining remaining-life parameters.

In this study, an analytical remaining-life approach is introduced to provide analytical solution of the remaining-life equation in addition to the existing numerical solution approach. By using two different solution approaches (i.e., two different ways of solving the remaining life equation), fatigue-crack growth simulations are performed for a 2024-T3 aluminum specimen with a pre-existing crack under various loading conditions i.e. different R ratios and stress levels. The remaining-life parameters are determined by calibrating model parameters with the experimental crack growth data of 2024-T3 aluminum alloy. Simulated results obtained by two approaches are assessed to determine their capabilities and shortcomings.

2. Peridynamic methodology

2.1. A review of peridynamic theory for elastic deformations

The PD theory is formulated in the form of an integro-differential equation which does not include spatial derivative in Eq. (1).

$$\rho(\xi)\ddot{\mathbf{u}}(\xi, t) = \int_H (\mathbf{t}(\boldsymbol{\eta}, \xi, t) - \mathbf{t}'(\boldsymbol{\eta}', \xi', t))dH + \mathbf{b}(\xi, t) \quad (1)$$

where ρ is mass density, \mathbf{u} and $\ddot{\mathbf{u}}$ are the displacement and acceleration, respectively. \mathbf{t} denotes the force density that the material point at \mathbf{x}' exerts on the material point at \mathbf{x} and, \mathbf{t}' represents the force density that the material point at \mathbf{x} exerts on the material point at \mathbf{x}' . dH is an incremental volume of the material point. ξ and $\boldsymbol{\eta}$ are the initial relative position vector and relative displacement vector in the reference configuration in Fig. 2, respectively. \mathbf{b} is a prescribed external body force density.

Thus, the PD equation can be applied to any type of discontinuities such as a crack tip or crack surfaces. The PD governing equation of Eq. (1) can be reformulated as the discretized form in Eq. (2).

$$\rho_{(k)} \ddot{\mathbf{u}}_{(k)} = \sum_{j=1}^N [\mathbf{t}_{(k)(j)}(\boldsymbol{\eta}_{(k)(j)}, \boldsymbol{\xi}_{(k)(j)}, t) - \mathbf{t}_{(j)(k)}(\boldsymbol{\eta}_{(j)(k)}, \boldsymbol{\xi}_{(j)(k)}, t)] V_{(j)} + \mathbf{b}_{(k)} \quad (2)$$

where \mathbf{N} denotes a number of family members of the material point, k and j denotes a specific family member of the material point, k . $V_{(j)}$ is an incremental volume of the material point.

As shown in Fig.2, the material point, $\mathbf{x}_{(k)}$ has a unique finite distance region called “horizon, δ ”. Within this horizon region, all material points interact with the material point, $\mathbf{x}_{(k)}$ on the basis of nonlocal interactions. It is also regarded that each material point possesses its own volume, $V_{(j)}$ for given configurations of the continuous material body. Figure 2 described a three-dimensional PD model in the undeformed and deformed states [53]. Let’s consider two interacting material points, $\mathbf{x}_{(k)}$ and $\mathbf{x}_{(j)}$ in the undeformed state. In the undeformed state, all of the position vectors constitute material body, and material points, $\mathbf{x}_{(k)}$ and $\mathbf{x}_{(j)}$ are relocated by displacement vector, $\mathbf{u}_{(k)}$ and $\mathbf{u}_{(j)}$ to the deformed state. In addition, two relative position vectors of the initial and current state, $\mathbf{x}_j - \mathbf{x}_k = \boldsymbol{\xi}_{(k)(j)}$ and $\mathbf{y}_j - \mathbf{y}_k = \boldsymbol{\xi}_{(k)(j)} + \boldsymbol{\eta}_{(k)(j)}$ can be defined by taking into account the two position vectors in the undeformed and deformed states, respectively. Considering these two vectors, the stretch between the material points of $\mathbf{x}_{(k)}$ and $\mathbf{x}_{(j)}$ can defined in Eq. (3)

$$s_{(k)(j)} = \frac{(|\boldsymbol{\eta}_{(k)(j)} + \boldsymbol{\xi}_{(k)(j)}| - |\boldsymbol{\xi}_{(k)(j)}|)}{\boldsymbol{\xi}_{(k)(j)}} \quad (3)$$

On the other hand, $\mathbf{t}_{(k)(j)}$ and $\mathbf{t}_{(j)(k)}$ in Eq. (2) are defined as the force density interacting between material points as shown in Fig. 3 [53]. They are obtained based on the relationship between the strain energy density and force density in Eq.(4a) and (4b) given for material points, $\mathbf{x}_{(k)}$ and $\mathbf{x}_{(j)}$, respectively [53].

$$\mathbf{t}_{(k)(j)}(\boldsymbol{\eta}_{(k)(j)}, \boldsymbol{\xi}_{(k)(j)}, t) = \frac{\mathbf{1}}{V_{(j)}} \frac{\partial W_{(k)}}{\partial(|\boldsymbol{\eta}_{(k)(j)} + \boldsymbol{\xi}_{(k)(j)}|)} \frac{\boldsymbol{\eta}_{(k)(j)} + \boldsymbol{\xi}_{(k)(j)}}{|\boldsymbol{\eta}_{(k)(j)} + \boldsymbol{\xi}_{(k)(j)}|} \quad (4a)$$

and

$$\mathbf{t}_{(j)(k)}(\boldsymbol{\eta}_{(j)(k)}, \boldsymbol{\xi}_{(j)(k)}, t) = \frac{\mathbf{1}}{V_{(k)}} \frac{\partial W_{(j)}}{\partial(|\boldsymbol{\eta}_{(j)(k)} + \boldsymbol{\xi}_{(j)(k)}|)} \frac{\boldsymbol{\eta}_{(j)(k)} + \boldsymbol{\xi}_{(j)(k)}}{|\boldsymbol{\eta}_{(j)(k)} + \boldsymbol{\xi}_{(j)(k)}|} \quad (4b)$$

Silling and Askari [47] defined a local damage in Eq. (5) to measure the crack formation stage. This method provides damage information as to how much the crack progresses without considering the configurations of material deformation. Local damage, φ has a range of 0 to 1. Herein, a value of 0 means a connected interaction between material points, and a value of 1 means a disconnected interaction between material points.

$$\varphi = 1 - \frac{\int_H \mu(\boldsymbol{\xi}_{(k)(j)}, t) dV_{(j)}}{\int_H dV_{(j)}} \quad (5)$$

where $\mu(\boldsymbol{\xi}_{(k)(j)}, t)$ is a history-dependent scalar-valued function to express the bond connection between material points in Eq. (6). If the stretch, $\mathbf{s}_{(k)(j)}$ is less than the critical stretch, \mathbf{s}_c , the material is deformed without damage, and if the stretch, $\mathbf{s}_{(k)(j)}$ is greater than the critical stretch, \mathbf{s}_c , the material is both deformed and damaged [53].

$$\mu(\boldsymbol{\xi}_{(k)(j)}, t) = \begin{cases} 1, & \text{if } \mathbf{s}_{(k)(j)}(\boldsymbol{\xi}_{(k)(j)}, t) < \mathbf{s}_c \text{ for all } 0 < t, \\ 0, & \text{otherwise} \end{cases} \quad (6)$$

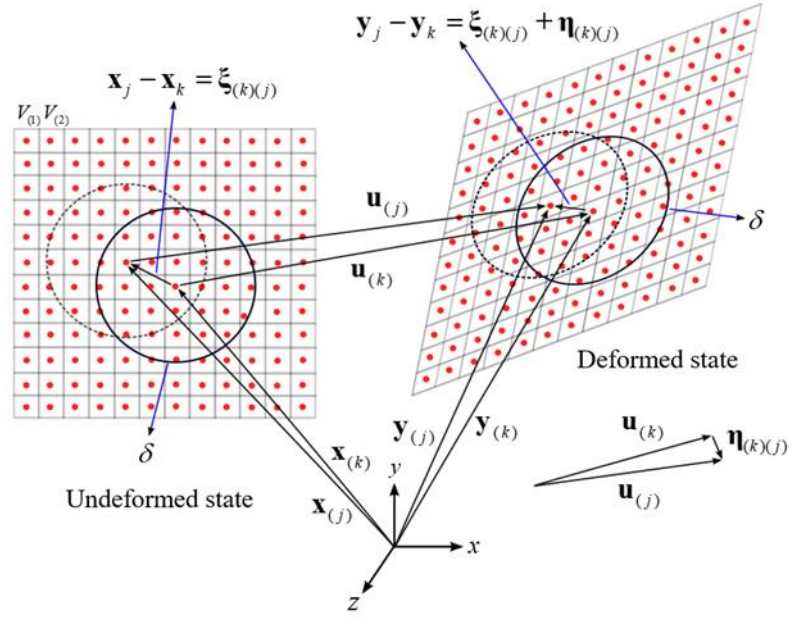


Fig. 2. Peridynamic interactions between material points, \mathbf{x}_k and \mathbf{x}_j in undeformed and deformed states.

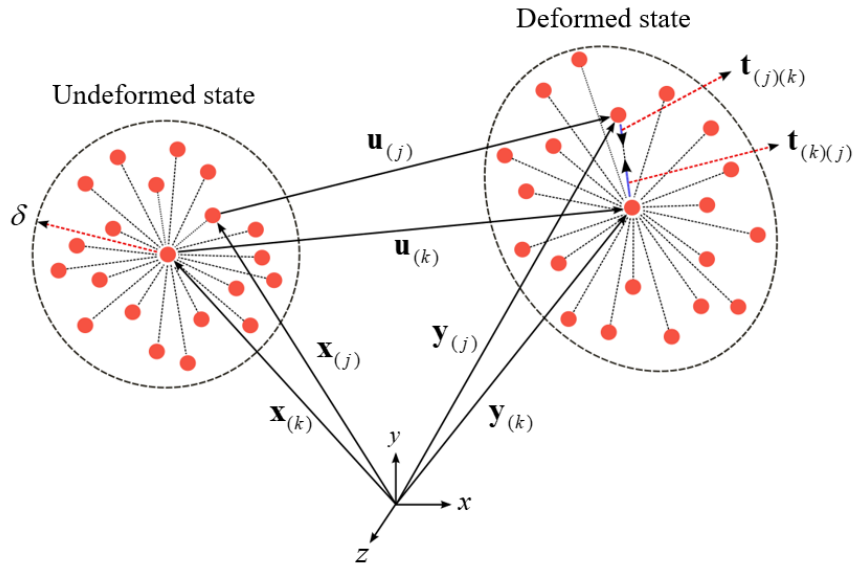


Fig. 3. Force densities acting at material points, \mathbf{x}_k and \mathbf{x}_j based on peridynamic interactions.

2.2. Peridynamic fatigue model

The PD fatigue model addresses elastic solid isotropic materials, and it can efficiently account for cumulative damages in a material body under cyclic loadings [48]. The main

advantage of the PD fatigue model is that both the crack nucleation and propagation states can be concurrently accounted for. In addition, the crack growth simulations and the material deformations can be performed on the basis of the real time.

To implement the PD fatigue model, the stretch which is defined at each point of extreme of loading cycles can be expressed in Eq. (7a) and (7b), respectively. Herein, the higher one is denoted " + " and the lower one is denoted as " - ".

$$s_{(k)(j)}^+ = \frac{(|\boldsymbol{\eta}_{(k)(j)}^+ + \boldsymbol{\xi}_{(k)(j)}| - |\boldsymbol{\xi}_{(k)(j)}|)}{\boldsymbol{\xi}_{(k)(j)}} \quad (7a)$$

and

$$s_{(k)(j)}^- = \frac{(|\boldsymbol{\eta}_{(k)(j)}^- + \boldsymbol{\xi}_{(k)(j)}| - |\boldsymbol{\xi}_{(k)(j)}|)}{\boldsymbol{\xi}_{(k)(j)}} \quad (7b)$$

By using the stretches of Eq. (7a) and (7b), "cyclic bond strain, $\varepsilon_{(k)(j)}$ " to represent the degree of deformations under fatigue loadings can be defined in Eq. (8). Also, the cyclic bond strain can be expressed as the right one of Eq. (8) by using the load ratio of $R = s_{(k)(j)}^- / s_{(k)(j)}^+$ which is determined based on the elastic material behaviors.

$$\varepsilon_{(k)(j)} = |s_{(k)(j)}^+ - s_{(k)(j)}^-| = |(1 - R)s_{(k)(j)}^+| \quad (8)$$

Thus, by employing the Eq. (8), Silling and Askari [48] established a remaining life equation of Eq. (9), which is defined as the instantaneous rate of remaining life over the time, t as a function of the cyclic bond strain, $\varepsilon_{(k)(j)}$. By applying the Eq. (9) to each bond between the material points, $\mathbf{x}_{(k)}$ and $\mathbf{x}_{(j)}$ within a horizon, gradually accumulated damages in the material body can be simulated.

$$\frac{d\lambda_{(k)(j)}}{dt} = -A(\varepsilon_{(k)(j)})^m \quad (9)$$

The first-order differential equation of the remaining-life equation, Eq. (9) has a value of unity for an initial condition (i.e., $\lambda_{(k)(j)}^0 = 1$) [48]. Also, the remaining-life equation in Eq. (9) can

be applied to both the crack nucleation and propagation phases. Therefore, the remaining-life parameters, A , m in Eq. (9) can be defined as A_1 , m_1 and A_2 , m_2 separately for the crack nucleation and propagation phases, respectively. In addition, the cyclic bond strain, $\varepsilon_{(k)(j)}$ in Eq. (9) increases under the cyclic loadings, and the corresponding remaining-life, $\lambda_{(k)(j)}$ decreases and eventually a bond breaks when the remaining-life is equal or less than zero, $\lambda_{(k)(j)} \leq 0$ as shown in Fig. 4 [48]. Herein, a bond just before it breaks is called “core bond”, and the core bond has the largest cyclic bond strain, ε_1 .

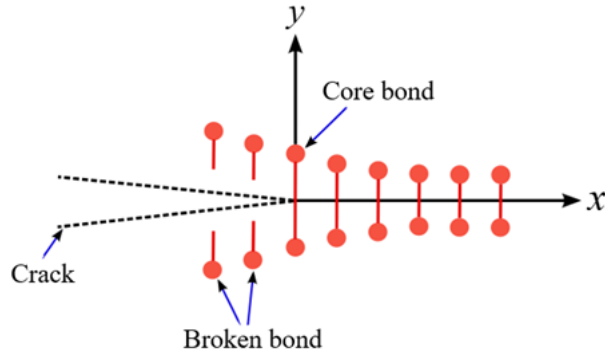


Fig. 4. Bond breakage at the crack tip.

On the other hand, the incremental time, t in Eq. (9) is a simulation time, not a real time. Therefore, by applying the linear mapping relationship in Eq. (10) and the chain rule in Eq. (11), the simulation time, t can be converted into the real-time loading cycle, N .

$$N = \frac{t}{\tau} \quad (10)$$

in which τ is a linear mapping constant.

$$\frac{d\lambda_{(k)(j)}}{dt} = \frac{d\lambda_{(k)(j)}}{dN} \frac{dN}{dt} \quad (11)$$

Thus, by using the Eq. (10) and (11), the remaining-life equation in Eq. (9) can be expressed in terms of the loading cycle, N in Eq. (12) for the crack nucleation phase.

$$\frac{d\lambda_{(k)(j)}}{dN} = -A_1 (\varepsilon_{(k)(j)})^{m_1} \quad , \quad \lambda_{(k)(j)}(0) = 1 \quad (12)$$

where the parameters, A_1 and m_1 are specified as $A_1 = A\tau$ and $m_1 = m$.

As for the crack nucleation phase, the variations of the cyclic bond strain, $\varepsilon_{(k)(j)}$ are very small under cyclic loadings. Thus, it can be assumed that the cyclic bond strain is independent of the loading cycle, N [48]. Therefore, based on this assumption, the remaining-life equation in Eq. (12) can be solved analytically as Eq. (13).

$$\lambda_{(k)(j)} = -A_1(\varepsilon_{(k)(j)})^{m_1}N + \lambda_{(k)(j)}(0) \quad (13)$$

where $\lambda_{(k)(j)}(0)$ is a value of unity. The crack is nucleated when the remaining life, $\lambda_{(k)(j)}$ is zero, and it occurs in the core bond. Thus, by employing the largest cyclic bond strain, ε_1 , the crack nucleation remaining-life expression can be written as Eq. (14).

$$A_1\varepsilon_1^{m_1}N = 1 \quad (14)$$

Herein, A_1 , m_1 are obtained by calibrating with the experimental fatigue life (i.e. S-N) data, e.g., Eq. (14) is plotted as Fig. 5, and it is compared with the S-N curve which is expressed in terms of strain, and the remaining-life parameters, A_1 , m_1 are determined accordingly [48]. As a result, the loading cycle, N_1 at which the crack nucleates can be obtained in Eq. (15).

$$N_1 = \frac{1}{A_1\varepsilon_1^{m_1}} \quad (15)$$

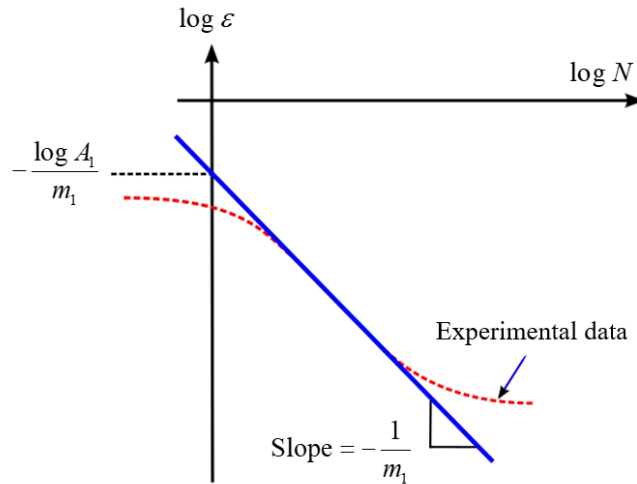


Fig. 5. Loading cycle, N_1 as a function of the largest bond strain, ε_1 for crack nucleation damage.

As for the crack propagation phase, by using the Eq. (10) and (11), the remaining-life equation of Eq. (9) can be expressed in terms of the loading cycle, N as Eq. (16).

$$\frac{d\lambda_{(k)(j)}}{dN} = -A_2(\varepsilon_{(k)(j)})^{m_2} \quad , \quad \lambda_{(k)(j)}(0) = 1 \quad (16)$$

where the parameters, A_2 and m_2 are specified as $A_2 = A\tau$ and $m_2 = m$. Herein, to determine the remaining-life parameters, A_2 and m_2 in Eq. (16), the PD crack growth rate expression should be described in the frame reference of the crack geometry [48]. To do that, the reference coordinate, z in Eq. (17) is defined to specify the location of the effectiveness length of the remaining-life within a horizon, δ and it has the range of 0 to δ (i.e., $0 \leq z \leq \delta$).

$$z = x - \frac{da}{dN}N \quad (17)$$

where a is crack length, and x is the coordinate along the crack growth axis. From the Eq. (17), it is known that the effective length, z and the crack length, a in the coordinate configuration are all dependent of the loading cycle, N , and it leads to Eq. (18).

$$\frac{da}{dN} = \frac{dz}{dN} \quad (18)$$

By using the coordinate, z in Eq. (17), the cyclic bond strain and remaining life defined between material points, $\mathbf{x}_{(k)}$ and $\mathbf{x}_{(j)}$ can be re-expressed as a function of the loading cycle, N in terms of the coordinate, z in Eq. (19).

$$\varepsilon_{(k)(j)}(N) = \bar{\varepsilon}_{(k)(j)}(z) \quad , \quad \lambda_{(k)(j)}(N) = \bar{\lambda}_{(k)(j)}(z) \quad (19)$$

where the cyclic bond strain, $\bar{\varepsilon}_{(k)(j)}(z)$ and remaining life, $\bar{\lambda}_{(k)(j)}(z)$ are defined for the range of $0 \leq z \leq \delta$. At this point, the remaining-life value is defined at the end of point for that range as in Eq. (20), and the cyclic bond strain is the core cyclic bond strain as $\bar{\varepsilon}_{(k)(j)}(0) = \varepsilon_{core}$ at the end of point, $z = 0$ [48].

$$\bar{\lambda}_{(k)(j)}(0) = 0, \quad \bar{\lambda}_{(k)(j)}(\delta) = 1 \quad (20)$$

Accordingly, consider the instantaneous value of the remaining-life and integrate it over the range of $0 \leq z \leq \delta$ and it leads to Eq. (21) using the expression of the chain rule.

$$\int_0^\delta d\lambda_{(k)(j)} = \int_0^\delta \frac{d\lambda_{(k)(j)}}{dN} \frac{dN}{dz} dz = 1 \quad (21)$$

Therefore, by substituting Eq. (16) and (18) for Eq. (21), the PD crack growth rate expression in terms of the loading cycle, N can be obtained in Eq. (22).

$$\frac{da}{dN} = A_2 \int_0^\delta \left(\bar{\epsilon}_{(k)(j)}(z) \right)^{m_2} dz \quad (22)$$

On the other hand, the bond strain, $s_{(k)(j)}(z)$ is defined in the z coordinate system by multiplying the core bond strain, s_{core} (i.e., the PD strain between the material points, $\mathbf{x}_{(k)}$ and $\mathbf{x}_{(j)}$ at the crack tip) by the arbitrary function of $f(z)$ as depicted in Eq. (23) [48].

$$s_{(k)(j)}(z) = s_{core} \times f(z) \quad (23)$$

where the arbitrary function of $f(z)$ has the value of one and zero at $z=0$ and $z=\delta$, respectively as $f(0) = 1$ and $f(\delta) = 0$.

To determine $f(z)$ in Eq. (23), apply the strain definition at the crack tip in the classical fracture mechanics to the PD core bond, the bond strain, $s_{(k)(j)}(z)$ in Eq. (23) can be described in terms of the stress intensity factor, K , young's modulus, E , the horizon, δ and the dimensionless proportional constant, \hat{s}_{bond} in Eq. (24)..

$$s_{(k)(j)}(z) = \hat{s}_{bond} \frac{K}{E\sqrt{2\pi z}} \quad (24)$$

Herein, Eq. (24) is defined when the coordinate, z goes to infinity (i.e., $z \rightarrow \infty$). In addition, based on the dimensional analysis, the core bond strain, s_{core} in Eq. (23) can be also described in terms of the stress intensity factor, K , young's modulus, E and the horizon, δ in Eq. (25).

$$s_{core} = \hat{s}_{core} \frac{K}{E\sqrt{\delta}} \quad (25)$$

where \hat{s}_{core} is a dimensionless proportional constant for the core bond strain.

Thus, by substituting Eq. (24) and (25) for Eq. (23), the function of $f(z)$ can be obtained in Eq. (26).

$$f(z) = \frac{1}{\hat{s}_{res} \sqrt{\frac{2\pi z}{\delta}}} \quad (26)$$

Herein, \hat{s}_{res} is a resultant dimensionless proportional constant obtained by dividing two proportional constants as $\hat{s}_{core}/\hat{s}_{bond}$.

To relate Eq. (22) and Eq. (26), the cyclic bond strain, $\bar{\varepsilon}_{(k)(j)}(z)$ can be expressed by multiplying the core cyclic bond strain, ε_{core} by the arbitrary function of $f(z)$ in Eq. (26) in the same way as Eq. (23).

$$\bar{\varepsilon}_{(k)(j)}(z) = \varepsilon_{core} \times f(z) \quad (27)$$

As a result, by using the Eq. (22), (26), and (27), the PD crack growth rate in terms of the remaining-life parameters, A_2 , m_2 , a horizon, δ , a resultant dimensionless proportional constant, \hat{s}_{res} , and the core cyclic bond strain, ε_{core} (which varies for the loading conditions at the crack tip), can be expressed in Eq. (28).

$$\frac{da}{dN} = \beta A_2 (\varepsilon_{core})^{m_2} \quad , \quad \beta = \frac{\delta^{(1-\frac{m_2}{2})}}{\left(\hat{s}_{res} \left(\frac{2\pi}{\delta}\right)^{\frac{1}{2}}\right)^{m_2} \left(1-\frac{m_2}{2}\right)} \quad (28)$$

where the core cyclic bond strain, ε_{core} is the value of the cyclic bond strain at $z=0$ when the bond breaks at the crack tip. Also, the cyclic bond strain, ε_{core} is related to the stress intensity factor range, ΔK of the LEFM, since these two quantities are linearly proportional to each other at the crack tip under the cyclic loading conditions. Therefore, by recalling the Paris law, Eq. (28) is related to $da/dN = C(\Delta K)^M$, and thus the exponent parameter in Eq. (28) can be described as $m_2 = M$ [48]. In addition, as for a determination of A_2 , it is not possible for the

Eq. (28) to be related to the Paris law, $da/dN = C(\Delta K)^M$, because the core cyclic bond strain, ε_{core} in Eq. (28) and the stress intensity factor range, ΔK in the Paris law are not identical, and the value of β in Eq. (28) cannot be found, because of the unknown resultant dimensionless proportional constant, \hat{s}_{res} in Eq. (28). Therefore, the remaining parameter, A_2 in Eq. (16) should be determined by an alternative way by considering the linear relationship of A_2 and the crack growth rate, da/dN . By using the arbitrary value of A' and its associated crack growth rate, $(da/dN)'$, A_2 is evaluated on the basis of the remaining-life solution in Eq. (29). Then, this evaluation is repeated until the PD predicted growth rate is fitted to the crack growth rate data.

$$A_2 = A' \frac{(da/dN)}{(da/dN)'} \quad (29)$$

where da/dN is the real data for crack growth rate, which can be obtained from experimental data or the Paris law.

2.3. Numerical and analytical remaining-life approaches

In order for the remaining-life solution to be used as the failure criterion in the PD fatigue model, the remaining-life equation should be solved. As for the crack nucleation phase, the remaining-life equation can be solved analytically by assuming that the cyclic bond strain is independent of the loading cycle, N , which is led by the fact that the variations of the cyclic bond strain is very small under the loading cycles. Whereas, as for the crack propagation phase, the cyclic bond strain is relatively larger than that of the nucleation phase. Therefore, the remaining-life equation can be solved numerically by taking into account the effects of the variations of the cyclic bond strain at every time step as shown in Eq. (30) [48].

$$\lambda_{(k)(j)}^n = \lambda_{(k)(j)}^{n-1} - A_2^{num} (\varepsilon_{(k)(j)}^n)^{m_2^{num}} \Delta N \quad , \quad \lambda_{(k)(j)}^0 = 1 \quad (30)$$

where n is the number of an iteration for remaining-life calculations. By using Eq. (30), the solutions of the remaining-life are updated numerically by evaluations at every time step.

Remaining-life value is the damage criterion for determining when the bond connection is broken by the bond force accumulated by cyclic loadings, i.e., the remaining life is the failure criterion for governing the crack growth under cyclic loadings. Therefore, there is no direct relationship between the remaining-life and the crack length. All bonds in the material experience changes in the remaining life, and the life of each bond is determined by the remaining life solution as shown in Fig. 6. In other words, remaining life begins to decrease from the point of unity with the increase of loading cycles, and when it reaches zero for the core bond (i.e. the most damaged bond in the vicinity of the crack tip.), the crack propagates one bond step due to breakage of the core bond. Figure 6 shows the process of remaining-life change for one single bond in the material.

The numerical remaining-life solutions of a center cracked tension (CCT) 2024-T3 aluminum specimen for different loading conditions of $R = 0/S_{\max} = 207$ MPa and $R = 0.33/S_{\max} = 155$ MPa are shown in Figs. 6a) and b). Herein, the remaining-life parameters of A_2^{num} , m_2^{num} obtained are depicted in Table. 1. As seen from the results in Figs. 6a) and b), it is found that the remaining-life solution by the numerical approach is stably converging from the initial point of unity for the loading condition of $R = 0/S_{\max} = 207$ MPa in Fig. 6a), whereas, the remaining-life is decreasing stepwise and converging unstably from the unity point under the loading conditions of $R = 0.33/S_{\max} = 155$ MPa in Fig. 6b). This shortcoming is attributed to the fact that the numerical solution of the remaining-life equation is limited to application of the fatigue simulation under different loading conditions. Therefore, in order to overcome this apparent shortcoming of the numerical approach for the PD fatigue model, a new approach is suggested to provide a potential solution of the remaining-life equation for crack propagation phase. The proposed solution approach is based on the assumption that remaining-life equation can be also solved analytically in a similar way to the nucleation phase.. Therefore, the effects of variations of the cyclic bond strain under the cyclic loadings can be disregarded. Thus, it can

be assumed that the cyclic bond strain is independent of the loading cycle, N in the crack propagation phase as well. Based on this assumption, the remaining-life equation can analytically be solved for the crack propagation phase as given in Eq. (31).

$$\lambda_{(k)(j)} = -A_2^{ana} (\varepsilon_{(k)(j)})^{m_2^{ana}} N + 1 \quad (31)$$

The obtained solution results from the analytical remaining-life solution in Eq. (31) are shown for different loading conditions of $R = 0/S_{\max} = 207$ MPa and $R = 0.5/S_{\max} = 138$ MPa in Figs. 6a) and b), respectively. Herein, the remaining-life parameters of A_2^{ana} , m_2^{ana} used are depicted in Table 1. As seen from, Figs. 6a) and b), unlike the results of the numerical approach, the remaining-life solution by the analytical approach is stably converging from the point of unity for different loading conditions. Furthermore, the analytical approach yields shorter computational time in comparison to the numerical approach in Figs. 6a) and b), respectively. A detailed comparison of the two approaches based on the crack growth distance, crack growth rates, and associated material deformation results with a growing crack will be discussed in section 3.

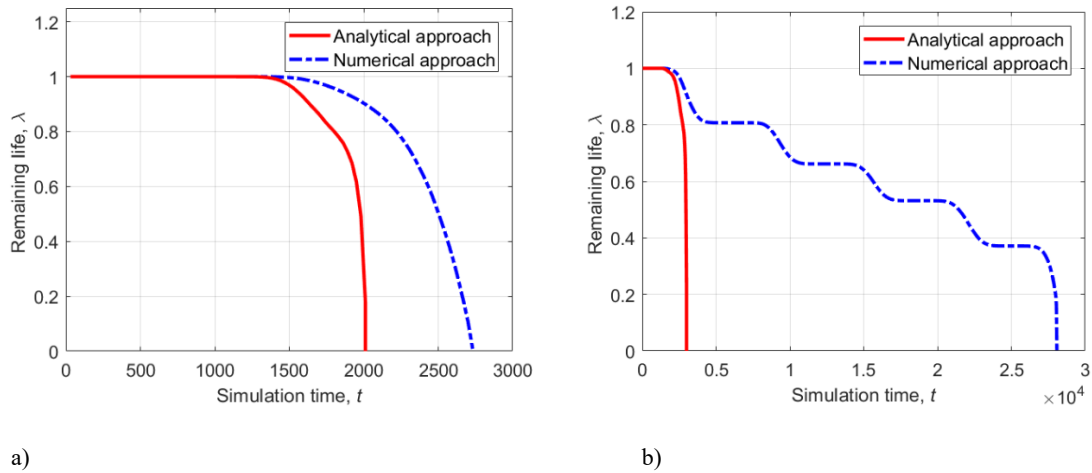


Fig. 6. Remaining life variations as a function of a simulation time, t in sec for the loading conditions of

a) $R=0$, $S_{\max} = 207$ MPa; b) $R=0.5$, $S_{\max} = 138$ MPa.

On the other hand, the remaining-life parameters of the numerical and analytical approaches, A_2^{num}, m_2^{num} and A_2^{ana}, m_2^{ana} in Eq. (30) and (31) are determined by the procedure described in section 2.2. The PD crack growth rate expression of the numerical and analytical approaches in Eq. (32a) and (32b) are related to the Paris law data [55], and the exponent parameters for each approach are determined as $m_2^{num} = m_2^{ana} = 4$ in Table 1. Herein, both exponent parameters have the same value of 4. Since the linear proportionality of the stress intensity factor range, ΔK and the core cyclic bond strain, ε_{core} at the crack tip are not affected by the magnitude of the core cyclic bond strain in Eq. (32a) and (32b), i.e., the exponent value of Eq. (32a) and (32b) are not changed by the different approaches of remaining-life conditions.

$$\frac{da}{dN} = \beta^{num} A_2^{num} (\varepsilon_{core})^{m_2^{num}} \quad (32a)$$

and

$$\frac{da}{dN} = \beta^{ana} A_2^{ana} (\varepsilon_{core})^{m_2^{ana}} \quad (32b)$$

where β^{num} and β^{ana} are prescribed as
$$\beta^{num} = \frac{\delta^{\left(1 - \frac{m_2^{num}}{2}\right)}}{\left(\dot{\varepsilon}_{res} \left(\frac{2\pi}{\delta}\right)^{\frac{1}{2}}\right)^{m_2^{num}} \left(1 - \frac{m_2^{num}}{2}\right)}$$

and
$$\beta^{ana} = \frac{\delta^{\left(1 - \frac{m_2^{ana}}{2}\right)}}{\left(\dot{\varepsilon}_{res} \left(\frac{2\pi}{\delta}\right)^{\frac{1}{2}}\right)^{m_2^{ana}} \left(1 - \frac{m_2^{ana}}{2}\right)}$$
 for the numerical and analytical approaches, respectively.

In addition, the remaining-parameters of A_2^{num} and A_2^{ana} are determined by calibrating with the experimental crack growth data for the numerical and analytical approaches, respectively.

This calibration process is repeated based on the linear relationship between the parameters of A_2^{num}, A_2^{ana} and the PD crack growth simulation results obtained from the numerical and analytical approaches, as given in Eq. (33a) and (33b), respectively.

$$A_2^{num} = (A')^{num} \frac{(da/dN)}{((da/dN)^r)^{num}} \quad (33a)$$

and

$$A_2^{ana} = (A')^{ana} \frac{(da/dN)}{((da/dN)^r)^{ana}} \quad (33b)$$

where da/dN is the real data for crack growth rate, and $(A')^{num}$ and $(A')^{ana}$ are the arbitrary values for the numerical and analytical approaches, respectively.

Since the remaining-parameters of A_2 (i.e. A_2^{num} and A_2^{ana}) are unknown in Eq. (32a) and (32b), the computed crack growth rate vs N cycle result cannot be obtained before the remaining-life solution is determined. Therefore, the remaining-life solution is computed by using an arbitrary value of A' i.e. $(A')^{num}$ and $(A')^{ana}$ in Eqs. 30 and 31. Then, the calculated crack growth rate in Eq. (32a) and (32b) is evaluated with the arbitrary value of A' at every time step, and it repeats until the predicted crack growth rate matches with the experimental data as given in Eq. (33a) and (33b), and the converged value of A_2 at that point is regarded as the parameter A_2 of the remaining-life equation. The parameter m_2 (i.e. m_2^{num} and m_2^{ana}) in Eq. (32a) and (32b) is directly obtained from the power constant of the Paris equation.

Table 1. Remaining-life parameters based on the numerical and analytical approaches for the 2024-T3 aluminum alloy.

	Remaining-life parameters	
Numerical approach	A_2^{num}	1150
	m_2^{num}	4
Analytical approach	A_2^{ana}	1300
	m_2^{ana}	4

2.4. Numerical implementation of analytical and numerical remaining-life solutions

The loading process of the PD fatigue model is implemented by applying the cyclic loadings to the body force of external force in the PD governing equation. The degree of

physical deformation of the material body is realized by the difference of the stretches at each bond into which the external force is transferred from the two extreme points of the loading cycles. To simulate fatigue-crack growth of the material body under the cyclic loadings, a bond interacting perpendicular to the crack growth axis for the growing crack model I is considered within a horizon. As the failure criterion for the crack growth simulation, the remaining-life is applied to each bond in the material body, which physically represents the cumulative damage obtained from a solution of the first-order differential equation of the remaining-life equation. Herein, the remaining-life equation is solved by setting the initial value of the solution at the length of horizon, δ which is the longest length that can be affected by the variations of the remaining life [48]. As a number of cyclic load increases, the remaining-life value decreases from the point of unity, and eventually when the value reaches to/less than zero, the bond breaks, and the crack growth is progressed as one iteration step. The extent to how much fast the remaining-life decreases in the remaining-life curve depends on both the magnitude and number of load cycles. The degree of decrease of the remaining-life value influences the behavior of the crack growth. As for the numerical approach, the remaining life is updated by reducing the size by a discrete length in every iteration step. Whereas, in case of the analytical approach, the remaining-life is determined directly by taking the analytical remaining-life solution corresponding to simulation time, t in every iteration step. The crack growth behavior on the basis of the PD fatigue model can be determined by two different approaches of the remaining-life method. A modeling algorithm of the peridynamic fatigue model on the basis of these two solution approaches is schematically shown in Fig. 7. The integro-differential equation of the PD governing equation under the cyclic loadings is solved at every time step by applying the Adaptive Dynamic Relaxation (ADR) method [54], and based on this iterative computation process, the remaining-life value is updated and evaluated at every iteration step.

The crack growth predictions obtained by the two approaches are based on the simulation time, not actual loading cycle, because the PD simulation is performed based on the simulation time, not real time. The simulation time generated by the PD fatigue model is well compatible with the convergence time produced by the ADR integrations. Therefore, the linear mapping technique which converts the simulation time into the actual loading cycles is very suitable for implementing the PD fatigue model. Note that one of the loading cycles to failure for specific ranges should be known in advance for the successfully application of the linear mapping technique [48]. Furthermore, the peridynamic simulation results (i.e. the crack growth length vs N cycle obtained from the PD fatigue model) are used to obtain the PD crack growth rate vs stress intensity factor range, ΔK . To do this, within a framework of LEFM, by using the maximum applied stress-level, S_{max} , geometry correction factor, Y in Eq. (34) (this study applies the CCT specimen) and the crack length, a of the PD results, the maximum stress intensity factor, K_{max} is calculated.

$$Y = \sqrt{\sec\left(\frac{\pi a}{w}\right)} \quad (34)$$

where a is crack length and w is a width of specimen.

Then, based on the maximum stress intensity factor, K_{max} , by using the stress ratio, R defined as the ratio of the minimum and maximum applied stress-levels at the extreme points of the cyclic loadings, the stress intensity factor range, ΔK can also be calculated. Accordingly, the PD crack growth rate vs N cycle can be obtained from the PD crack growth length vs N cycle computed by the PD fatigue model. However, as mentioned above, the crack growth behaviors are quite dependable to the magnitude of the remaining-life parameters and the solution approach of the remaining-life equation. Thus, the computed crack growth rate is also dependent to the magnitude of the remaining-life parameters of A_2, m_2 . Therefore, the remaining-life parameters of A_2^{num}, m_2^{num} and A_2^{ana}, m_2^{ana} for the numerical and analytical

approaches are determined such that, the PD crack growth rate is calculated by using the arbitrary value of $(A')^{num}, (A')^{ana}$ based on the crack growth length vs N cycle result. The calculated values are compared at every time step to the experimental data with updated values of $(A')^{num}, (A')^{ana}$. And finally, when the crack growth rate results are fitted to the experimental data, the parameters, $(A')^{num}, (A')^{ana}$ are determined for numerical and analytical approaches, respectively (see the flow chart in Fig. 7). On the other hand, the exponent parameters of m_2^{num}, m_2^{ana} for two approaches are directly obtained from the Paris law power constant. The convergence criterion, R for whether the crack growth rate agrees well with the experimental data is evaluated by comparing the absolute value of the difference between the experimental crack growth data and predicted model results in Eq. (35). If the absolute value of the difference is less than $R=0.0001$ [mm/cycle], the model predictions are considered to be in agreement with the experimental data.

$$\left| \left(\frac{da}{dN} \right)^{PD} - \left(\frac{da}{dN} \right)^{Exp} \right| \leq R \quad (35)$$

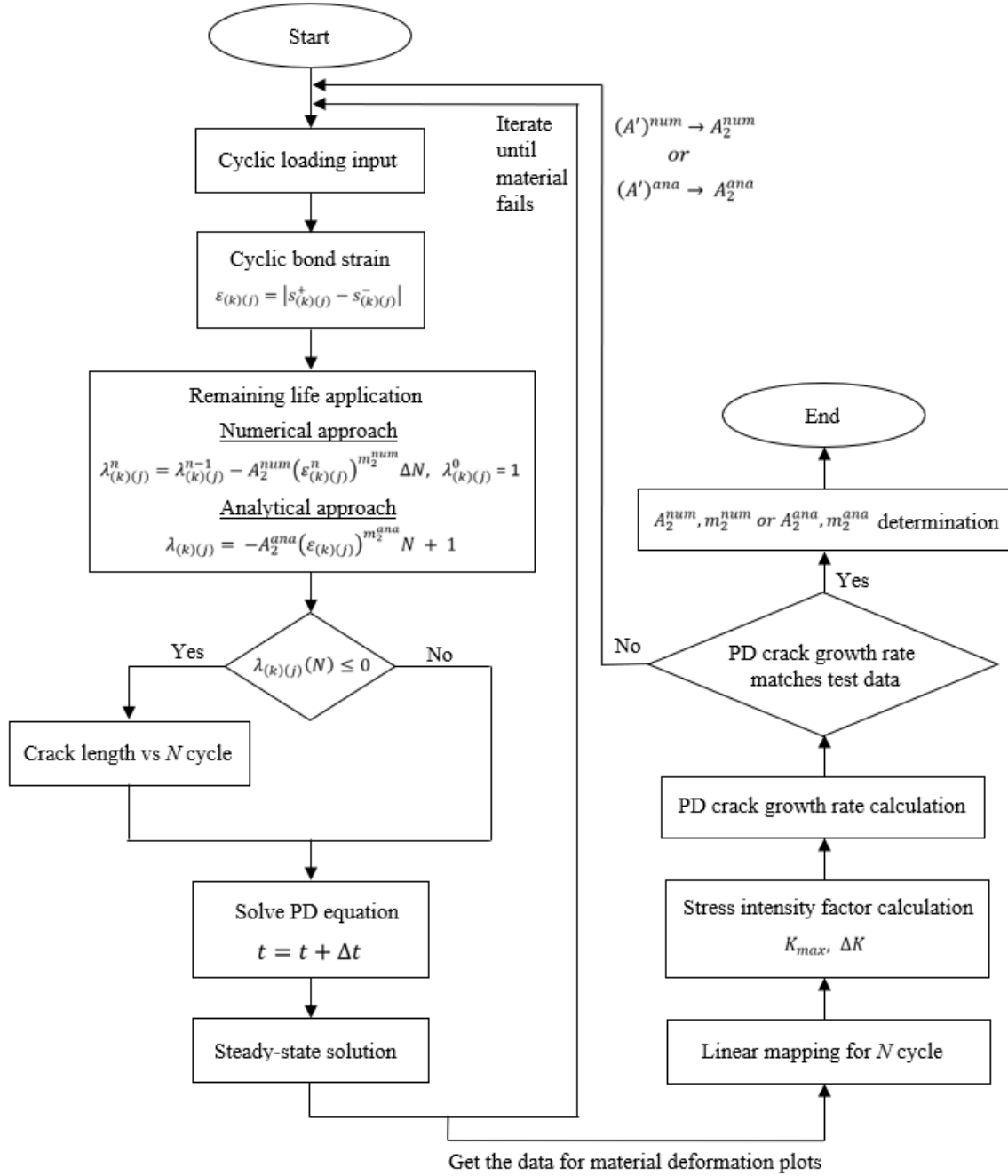


Fig. 7. Flow chart of fatigue-crack growth simulation using a peridynamic fatigue model at a pre-existing crack.

3. Crack growth results at a pre-existing crack

A center cracked tension (CCT) specimen for 2024-T3 aluminum alloy is adopted to model and simulate the PD fatigue-crack growth [55]. The 2024-T3 aluminum alloy has Young's modulus of $E = 73.0 \text{ GPa}$, mass density of $\rho = 2780 \text{ kg/m}^3$, and Poisson's ratio of $\nu = 0.33$, and the CCT specimen is presented with a width of 305.0 mm, a length of 699.0

mm, and a thickness of 2.28 mm, and its notch is located with 0.25 mm by 2.54 mm in the center of the specimen as shown in Fig. 8. As for PD modeling of the plate specimen shown in Fig.8, the plate is discretized into 150×350 material points with a uniform grid. A constant horizon size is used as $\delta=3.015 \times \Delta$ m, in which Δ represents spacing between material points as $\Delta=0.002$ m. Initial crack size is regarded as $L=0.0025$ m, which is greater than Δ close to a specified notch size.

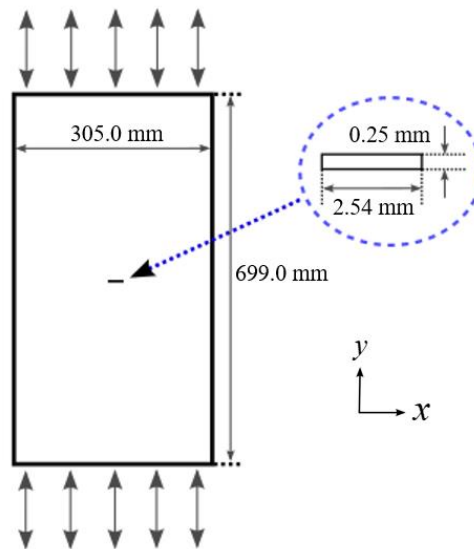


Fig. 8. Configuration of the center cracked tension specimen for 2024-T3 aluminum alloy.

3.1. Numerical solution approach for crack propagation

Figure 9 shows the fatigue-crack growth results obtained by applying the numerical remaining-life solution under four different loading conditions for the CCT 2024-T3 aluminum specimen. It is shown that the crack begins to grow the fastest under the loading condition of $R = 0 / S_{\max} = 207$ MPa, and then progressively at $R = 0.33 / S_{\max} = 155$ MPa and $R = 0.7 / S_{\max} = 241$ MPa, and the crack begins to grow the latest at $R = 0.5 / S_{\max} = 138$ MPa. Herein, the x axis in the coordinate is expressed as the actual loading cycle, N by applying the linear mapping technique. Computational time in seconds for each curve crack length versus loading cycle, i.e. $a-N$ is depicted in the caption of Fig. 9.

As can be seen from the results in Fig. 9, the crack growth results show non-smooth curves for the loading conditions of $R = 0.33/S_{\max} = 155$ MPa, $R = 0.5/S_{\max} = 138$ MPa, and $R = 0.7/S_{\max} = 241$ MPa, and as for the loading condition of $R = 0/S_{\max} = 207$ MPa the crack growth result shows a smooth a-N curve. This is attributed to the fact that two results are different is that the remaining-life parameter, A_2^{num} which dominates crack growth behavior is determined based on the crack growth data of $R = 0/S_{\max} = 207$ MPa in Fig.9.

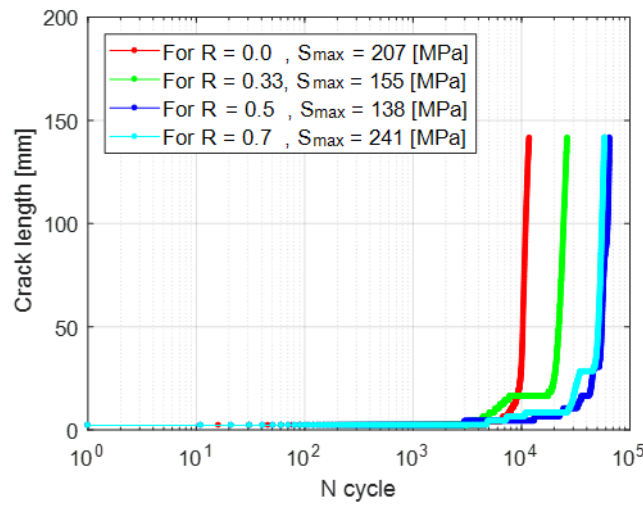


Fig. 9. Fatigue-crack growth curves for 2024-T3 aluminum alloy under different loading conditions. Computational time for a-N curves: 3061sec for $R = 0/S_{\max} = 207$ MPa; 10891sec for $R = 0.33/S_{\max} = 155$ MPa; 40801sec for $R = 0.5/S_{\max} = 138$ MPa; 17281sec for $R = 0.7/S_{\max} = 241$ MPa

To predict the crack growth rate based on the fatigue-crack growth curve of Fig. 9, the remaining parameters, A_2^{num}, m_2^{num} must be determined from fatigue data of 2024-T3 aluminum alloy; m_2^{num} is obtained directly from the Paris law data [55], and A_2^{num} is determined by calibrating with the experimental crack growth data [55] for the loading condition of $R = 0/S_{\max} = 207$ MPa in Fig. 10a). Note that experimental data of different loading conditions in Fig. 10 can be utilized to determine the remaining parameter of A_2^{num} . However, in that case, different values of the remaining parameter are determined for each loading condition. The remaining-life parameters shown in Table 1 are obtained from the crack growth data of 2024-T3 aluminum alloy under the loading condition of $R = 0/S_{\max} =$

207 MPa. Based on these parameters, the crack growth rates for other loading conditions of $R = 0.33/S_{\max} = 155$ MPa, $R = 0.7/S_{\max} = 241$ MPa and $R = 0.5/S_{\max} = 138$ MPa are predicted from the crack length curves in Fig. 9 on the basis of the numerical solution approach. However, it can be seen that the predicted crack growth rates are not correlated well with the experimental data for the loading conditions of $R = 0.33/S_{\max} = 155$ MPa, $R = 0.5/S_{\max} = 138$ MPa and $R = 0.7/S_{\max} = 241$ MPa as shown in Figs. 10 b), c) and d), respectively. These predicted results show that the numerical solution approach has prediction limitations for general loading conditions other than the load condition from which the remaining life parameters are determined.

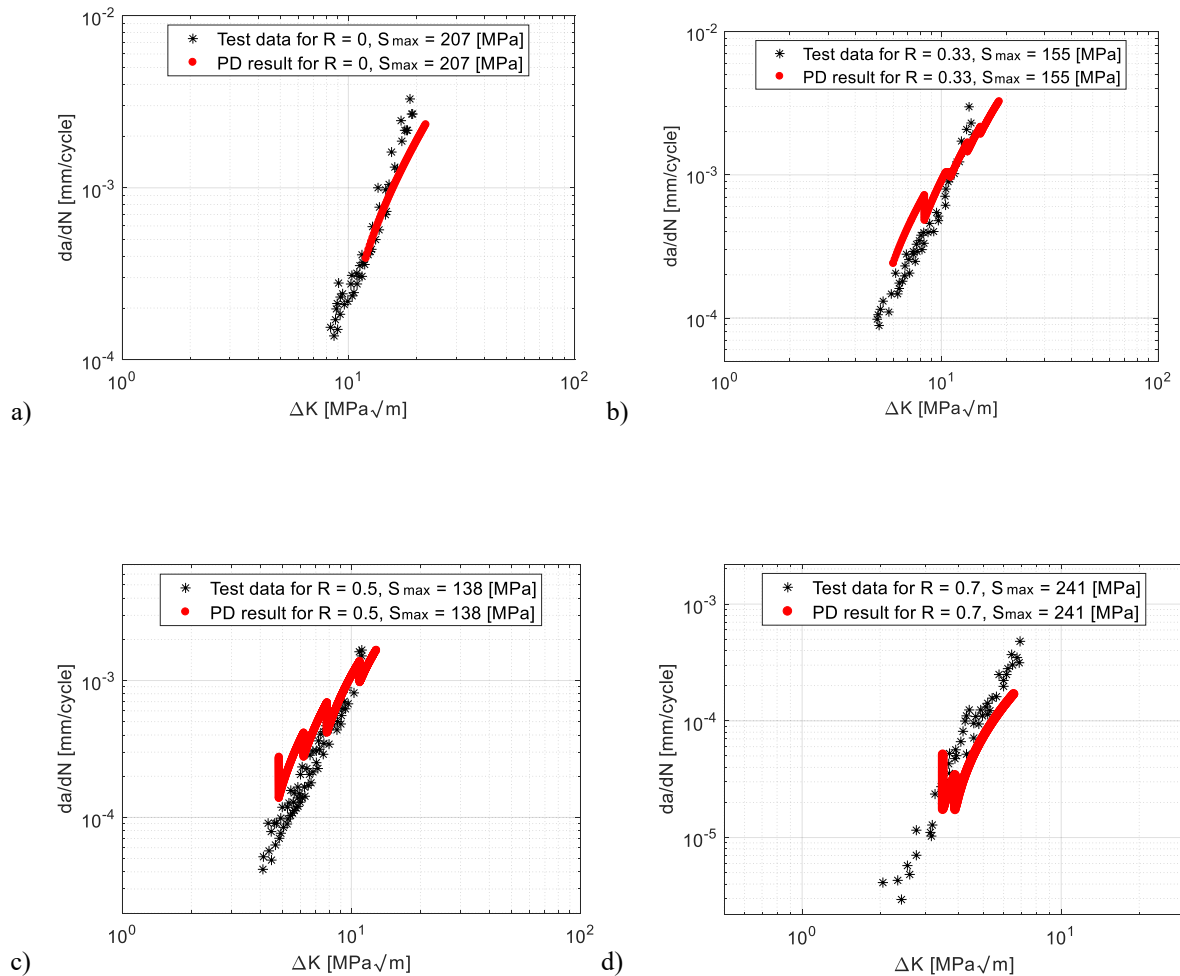
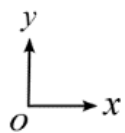


Fig. 10. Predicted crack growth rate and comparison with experimental data for 2024-T3 aluminum alloy under different loading conditions: a) $R = 0 / S_{\max} = 207$ MPa; b) $R = 0.33 / S_{\max} = 155$ MPa; c) $R = 0.5 / S_{\max} = 138$ MPa; d) $R = 0.7 / S_{\max} = 241$ MPa.

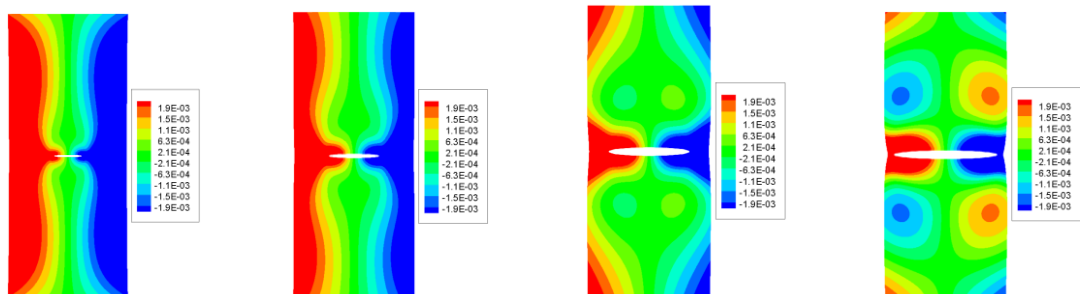
Figure 11 shows the simulation results for material deformation along with a growing crack in real time for 2024-T3 aluminum alloy for the loading condition of $R = 0.33 / S_{\max} = 155$ MPa. Deformation results of the CCT specimen with the crack evolution are demonstrated by applying a displacement exaggeration factor of 30 to make the crack shape visible. Figure 11 A and B shows the displacement results for material deformation with a growing crack at the loading condition of $R = 0.33 / S_{\max} = 155$ MPa in the x and y directions, respectively. Displacement changes are observed by irregular contour patterns in the material body when the loading cycle, N reaches the final stage of $N = 26580$ as shown in Fig. 11A. As a result, it is found that it is not possible to perform a stable simulation with a growing crack by the numerical approach for the loading condition of $R = 0.33 / S_{\max} = 155$ MPa.

Consequently, it is regarded that the numerical approach of the PD fatigue model is limited to its application for crack growth simulation under various loading conditions.



(Origin is located at the center of a crack)

A.



a) Crack length: 53mm
Loading cycles: 22530

b) Crack length: 81 mm
Loading cycles: 23880

c) Crack length: 109 mm
Loading cycles: 25170

d) Crack length: 141 mm
Loading cycles: 26580

B.

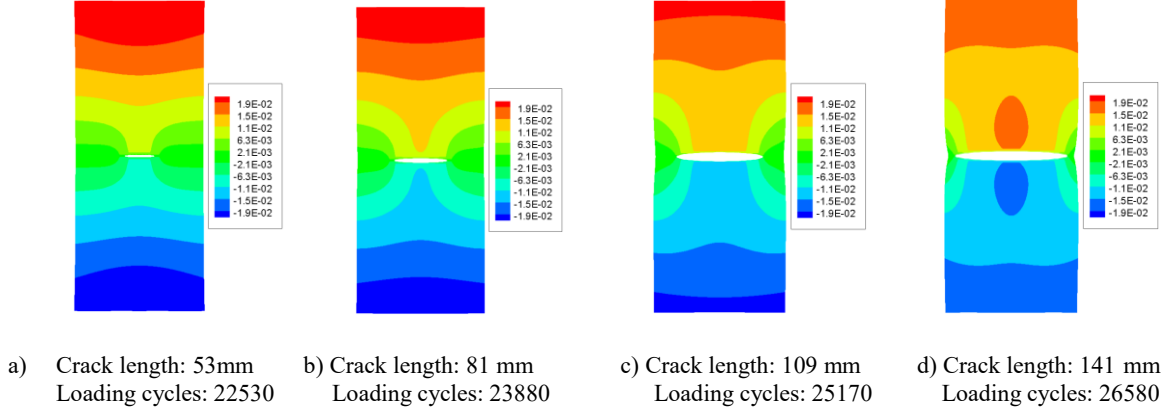


Fig. 11. Fatigue-crack growth simulation at $R = 0.33/S_{\max} = 155$ MPa for 2024-T3 aluminum alloy. Figure A. shows the displacement in the x direction (unit: mm); Figure B. shows the displacement in the y direction (unit: mm); displacement is exaggerated with a factor of 30.

3.2. Analytical solution approach for crack propagation

It is shown that the numerical approach of the PD fatigue model has shortcomings in its application for a wide range of loading conditions. This section provides a potential solution that addresses the shortcomings of the numerical approach by presenting predicted crack growth results on the basis of the analytical remaining-life approach thus demonstrating its prediction capabilities over the numerical solution approach. The remaining-life parameter, A_2^{ana} is determined by calibrating with the experimental crack growth data for the loading condition of $R = 0/S_{\max} = 207$ MPa, and the parameter, m_2^{ana} is obtained directly from the Paris law data [55]. The remaining-life parameters obtained here for 2024-T3 aluminum alloy for the analytical approach are given in Table 1.

Figure 12. shows the fatigue-crack growth length results obtained by applying the analytical remaining-life solutions for four different loading conditions for the CCT 2024-T3 aluminum specimen. Predicted a-N curves under four different loading conditions of $R = 0/S_{\max} =$

207 MPa, $R = 0.33/S_{\max} = 155$ MPa, $R = 0.7/S_{\max} = 241$ MPa, and $R = 0.5/S_{\max} = 138$ MPa are shown in Fig. 12. It is observed that predicted crack growth rate under the loading conditions of $R = 0.33/S_{\max} = 155$ MPa, $R = 0.7/S_{\max} = 241$ MPa, and $R = 0.5/S_{\max} = 138$ MPa agree well with the experimental data as shown in Figs. 13 b), c) and d). This result demonstrates that the crack growth rates can be predicted with reasonable accuracy by the analytical remaining-life approach for various loading conditions. As seen from the captions in Figs. 9 and 12, the computational time for performing crack growth simulation is considerably shorter compared to the numerical remaining-life approach.

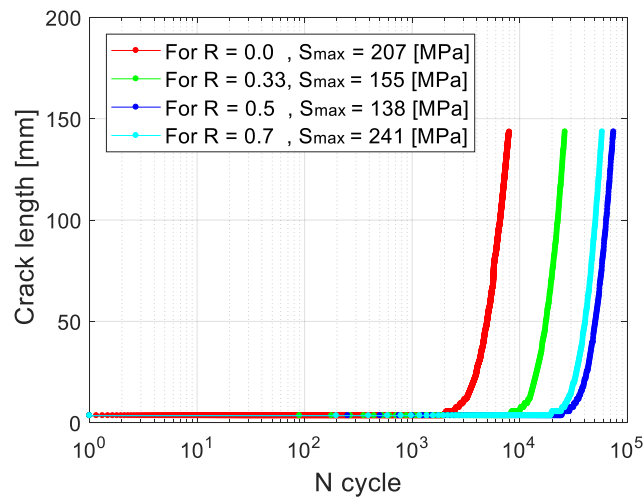
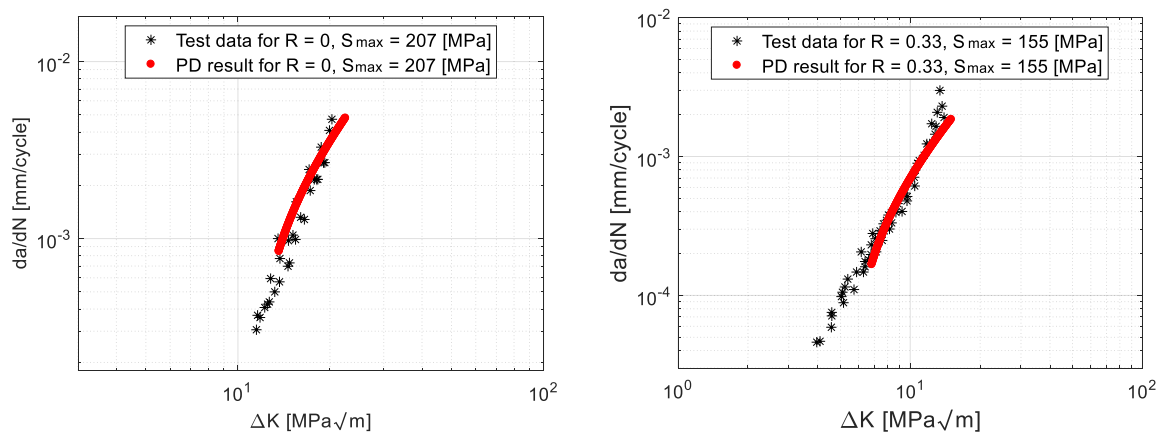


Fig. 12. Fatigue-crack growth curves for 2024-T3 aluminum alloy under different loading conditions. Computational time for developing curves: 3090sec for $R = 0/S_{\max} = 207$ MPa; 3811sec for $R = 0.33/S_{\max} = 155$ MPa; 4621sec for $R = 0.5/S_{\max} = 138$ MPa; 4081sec for $R = 0.7/S_{\max} = 241$ MPa



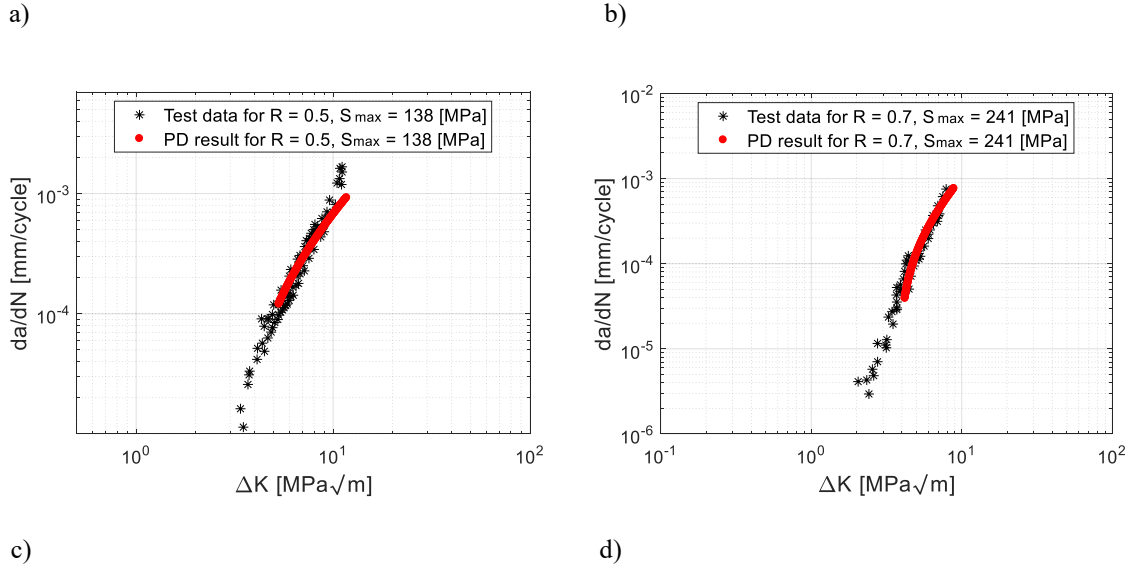


Fig. 13. Predicted crack growth rate and comparison with experimental data for 2024-T3 aluminum alloy under different loading conditions: a) $R = 0 / S_{\max} = 207$ MPa; b) $R = 0.33 / S_{\max} = 155$ MPa; c) $R = 0.5 / S_{\max} = 138$ MPa; d) $R = 0.7 / S_{\max} = 241$ MPa.

Figure 14 shows the results of material deformation with a growing crack in real simulation time under the loading condition of $R = 0.33 / S_{\max} = 155$ MPa. Figures 14 A and B show the material displacement results with a growing crack under the loading conditions of $R = 0.33 / S_{\max} = 155$ MPa for 2024-T3 aluminum alloy in the x and y directions, respectively. As can be seen in each plot of Figs. 14 A and B, it is considered that the displacement is stably evolved in the x and y directions as the load cycle increases. Consequently, it is regarded that the analytical approach can perform the fatigue-crack growth simulations for various loading conditions in a stable manner of the material deformation with a growing crack as shown in Figs 12-14. In addition, computational solution time of the analytical approach is significantly shorter than the numerical approach.

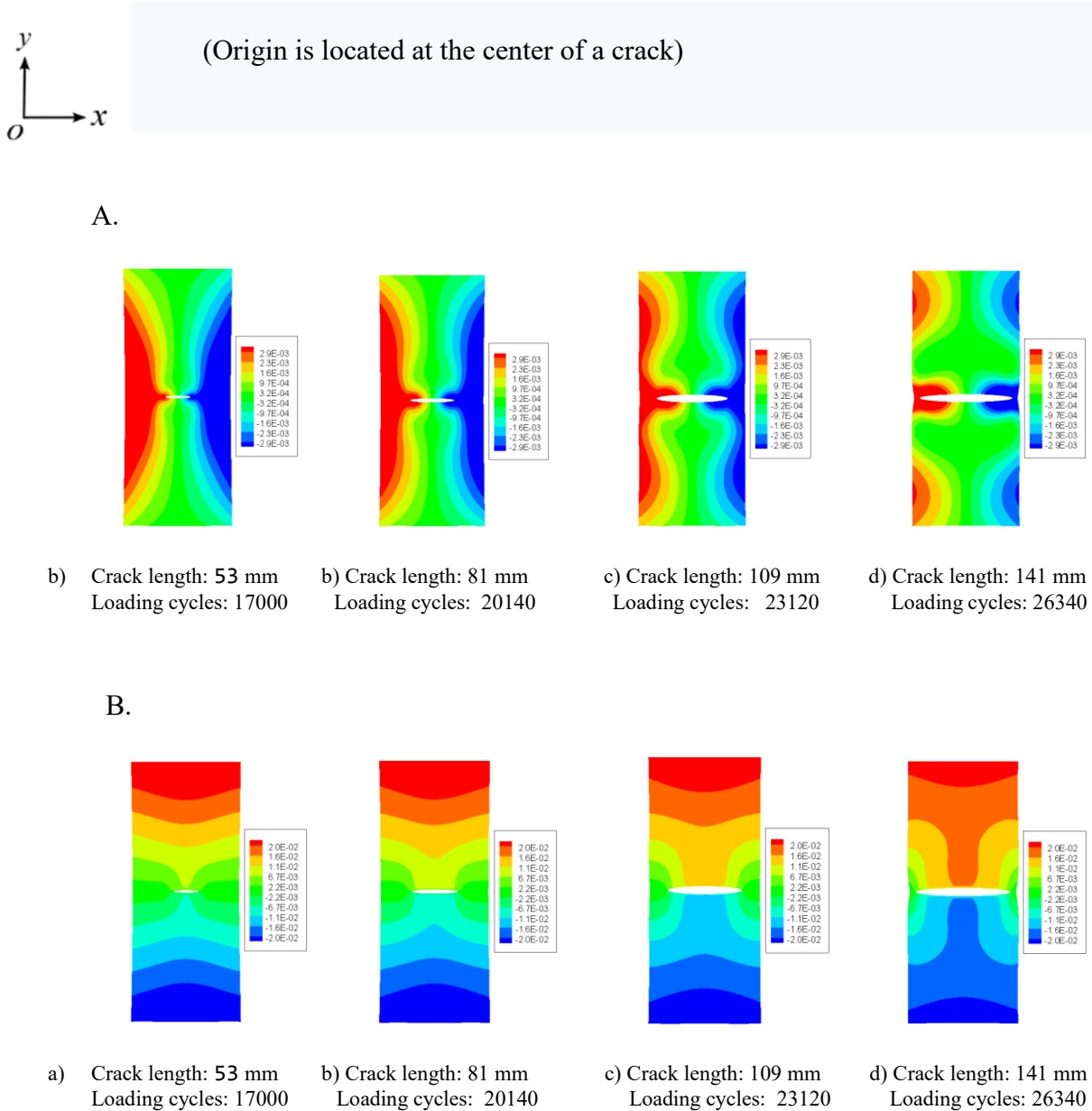


Fig. 14. Fatigue-crack growth simulation at $R = 0.33/S_{\max} = 155$ MPa for 2024-T3 aluminum alloy. Figure A. shows the displacement in the x direction (unit: mm); Figure B. shows the displacement in the y direction (unit: mm). Displacement is exaggerated with a factor of 30.

4. Conclusion

The analytical solution approach for the remaining-life method is introduced for providing the effective solution of the PD fatigue damage model. Predicted crack growth simulations have been implemented on the basis of both the analytical and numerical solution

approaches of the remaining-life method. It was found that the crack growth rates predicted by the numerical approach generate non-smooth crack growth a-N curves and the numerical approach provides poor correlations with the experimental data under different loading conditions. Furthermore, simulated material deformations showed irregular displacement fields on the deformation results. Whereas, the analytical approach yields smooth crack growth curves and the predicted crack growth rates are found to be in good agreement with the experimental data under different loading conditions. Furthermore, the material deformations are quite stably simulated by the analytical approach. It is also found that the computational time required for fatigue-crack growth simulations predicted by the analytical approach are considerably shorter than the numerical approach.

References

- [1] W. Gerber (1874) Bestimmung der zulossigen eisen construcionen. Z. Bayer Arch. Ing Ver.6, pp.101–110.
- [2] K. N. Smith, P. Watson, T.H. Topper (1970) A stress-strain function for the fatigue of materials, J. Mater.5, pp.767–778.
- [3] D.F. Socie and J.D. Morrow (1980) Review of Contemporary Approaches to Fatigue Damage Analysis. Risk and Failure Analysis for Improved Performance and Reliability. J. J. Burke and V. Weiss, eds., Plenum Pub. Corp. New York, NY, 141–194.
- [4] S.S. Manson, and G.R. Halford (1981) Practical implementation of the double linear damage rule and damage curve approach for treating cumulative fatigue damage. Int. J. Fract. Vol.17, pp.169–172.
- [5] A. Ince, and G. Glinka. (2011) A modification of Morrow and Smith-Watson-Topper mean stress correction models, Fatigue and Fracture of Engineering Materials and Structures Vol. 34, pp. 854–867.
- [6] A. Ince, and G. Glinka (2014) A generalized damage parameter for multiaxial fatigue life prediction under proportional and non-proportional loadings, Int. J. Fatigue, Vol. 62, pp.34–41.
- [7] P.C. Paris, H. Tada, J.K Donald (1999). Service load fatigue damage—a historical perspective. International Journal of Fatigue Vol. 21, pp.35–46.
- [8] D.J. Bang, A. Ince, M. Noban (2019). Modeling approach for a unified crack growth model in short and long fatigue crack regimes. Int. J. Fatigue. 128:105182.
- [9] D.J. Bang, A. Ince (2020). A short and long crack growth model based on 2-parameter driving force and crack growth thresholds. Int. J. Fatigue. 141: 105870.
- [10] A. Trädegård, F. Nilsson, S. Östlund (1998) Fem-remeshing technique applied to crack growth problems, Comput Methods Appl Mech Eng, Vol.160, pp.115-131.
- [11] P.O. Bouchard, F. Bay, Y. Chastel, I. Toven (2000) Crack propagation modelling using an advanced remeshing Technique, Comput. Methods Appl. Mech. Engrg, Vol.189, pp.723–742.
- [12] Y.S. Kim, S.H. Yang, D. Shan, S.O. Choi, S.M. Lee, B.S. You (2006) Three-Dimensional Rigid-Plastic FEM Simulation of Metal Forming Processes, J. Mater, Vol.15, pp.275-279.
- [13] L. Duchêne, F. E. Houdaigui, A. M. Habraken, (2007) Length changes and texture prediction during free end torsion test of copper bars with FEM and remeshing techniques, Int. J. Plast, Vol.23 pp.1417–1438.
- [14] A. M.P. de Jesus, A. L.L. da Silva, M. V. Figueiredo, J. A.F.O. Correia, A.S. Ribeiro, A.A.

- Fernandes (2011) Strain-life and crack propagation fatigue data from several Portuguese old metallic riveted bridges, *Eng. Fail. Anal.*, Vol.18, pp.148–163.
- [15] E. H. K.H. Chang, I. Grindeanu, S.p. Yoon, M. Kaneko, J.S. Chen (1999) A Structural Nonlinear Analysis Workspace (SNAW) based on meshless methods, *Adv. Eng. Softw.*, Vol.30, pp.153–175.
- [16] B.N. Rao and S. Rahman (2001) A coupled meshless-finite element method for fracture analysis of cracks, *International journal of pressure vessels and piping*, Vol.78, pp.647-657.
- [17] D. Marc and N.D. Hung (2004) A meshless method with enriched weight functions for fatigue crack growth, *Int. J. Numer. Meth. Engng.*, Vol. 59, pp.1945–1961.
- [18] Y.T. Gu, Q.X. Wang, K.Y. Lam (2007) A meshless local Kriging method for large deformation analyses, *Comput. Methods Appl. Mech. Engrg.*, Vol.196, pp.1673–1684.
- [19] E. Barbieri, N. Petrinic, M. Meo, V. L.Tagarielli (2012) A new weight-function enrichment in meshless methods for multiple cracks in linear elasticity, *Int. J. Numer. Meth. Engng.*, Vol. 90, pp.177–195.
- [20] T. Belytschko, T. Black (1999) Elastic crack growth in finite elements with minimal remeshing, *Int J Numer Meth Eng*, Vol.45, pp.601–620.
- [21] N. Moes, J. Dolbow, T. Belytschko (1999) A finite element method for crack growth without remeshing, *Int J Numer Meth Eng*, Vol.46, pp.131–150.
- [22] S.A. Silling (2000) Reformulation of elasticity theory for discontinuities and long-range forces. *J Mech Phys Solids*, Vol.48, pp.175–209
- [23] S.A. Silling, M. Epton, O.Weckner, J. Xu, A. Askari (2007) Peridynamics states and constitutive modeling. *J Elast*, Vol,88, pp.151–184.
- [24] E. Askari, J. Xu, S.A. Silling (2006) Peridynamic analysis of damage and failure in composites. Paper 2006–88 presented at the 44th AIAA aerospace sciences meeting and exhibit.Grand Sierra Resort Hotel, Reno, 9–12 Jan 2006.
- [25] J. Xu, A. Askari, O. Weckner, S.A. Silling (2008) peridynamic analysis of impact damage in composite laminates, *J. Aerosp. Eng.* Vol.21, pp.187-194.
- [26] E. Oterkus and E. Madenci (2012) Peridynamic analysis of fiber-reinforced composite materials, *Mech Adv Mater Struc*, Vol.7, pp.45-84.
- [27] C. Diyaroglu, E. Oterkus, E. Madenci, T. Rabczuk, A. Siddiq (2016) Peridynamic modeling of composite laminates under explosive loading, *Compos. Struct*, Vol.144, pp.14–23.
- [28] A. John. A. Mitchell (2011) Nonlocal, ordinary, state-based plasticity model for peridynamics, Sandia Report SAND2011-3166, Sandia National Laboratories, Albuquerque, NM, May 2011.
- [29] E. Madenci and Selda Oterkus (2016) Ordinary state-based peridynamics for plastic deformation according to von Mises yield criteria with isotropic hardening, *J. Mech. Phys.Solids*, Vol.86, pp.192–219.
- [30] S.A. Silling, F. Bobaru (2005) Peridynamic modeling of membranes and fibers, *Int J Nonlin Mech*, Vol.40, pp.395–409.
- [31] D.J. Bang and E. Madenci (2017) Peridynamic Modeling of Hyperelastic Membrane Deformation, *J Eng Mater-T ASME*, Vol. 139, 10 pages.
- [32] J.A. Mitchell (2011) A non-local, ordinary-state-based viscoelasticity model for peridynamics. Sandia National Lab., Report 8064, pp.1–28.
- [33] M.A. bin Azizi , A.K.A. bin Mohd Ihsan, N.A. bin Nik Mohamed (2015) The peridynamic model of viscoelastic creep and recovery, *Multidiscip*, Vol. 11, pp.579-597.
- [34] E.Madenci and S.Oterkus, (2017) Ordinary state-based peridynamics for thermoviscoelastic deformation, *Eng. Fract. Mech*, Vol.175, pp.31-45.
- [35] O. Weckner and N.A.N. Mohamed (2013) Viscoelastic material models in peridynamics. *Appl. Math. Comput*, Vol. 219, pp.6039–6043.
- [36] J.T. Foster, S.A. Silling, W.W. Chen (2010) Viscoplasticity using peridynamics, *Int. J. Numer Meth.Engng*, Vol. 81, pp.1242–1258.
- [37] H. Wang, Y. Xu, D. Huang (2019) A non-ordinary state-based peridynamic formulation for thermo-visco-plastic deformation and impact fracture, *Int. J. Mech. Sci*, Vol.159, pp.336–344.
- [38] F. Bobaru, M. Duangpanya (2010) The peridynamic formulation for transient heat conduction, *International Journal of Heat and Mass Transfer*, Vol.53, pp.4047–4059.
- [39] F. Bobaru, M. Duangpanya (2012) A peridynamic formulation for transient heat

- conduction in bodies with evolving discontinuities, *Journal of Computational Physics*, Vol.231, pp.2764-2775.
- [40] C. Diyaroglu, S. Oterkus, E. Oterkus, E. Madenci (2017) Peridynamic modeling of diffusion by using finite-element analysis, *IEEE Trans Compon Packaging Manuf Technol*, Vol.7, pp.1823-1831.
- [41] T. Xue, X. Zhang, K.K. Tamma (2018) A two-field state-based Peridynamic theory for thermal contact problems, *Journal of Computational Physics*, Vol. 374, pp.1180–1195.
- [42] Y. Tan, Q. Liu, L. Zhang, L. Liu, X. Lai (2020) Peridynamics model with surface correction near insulated cracks for transient heat conduction in functionally graded materials, *Mater.* Vol. 13, DOI: 10.3390/ma13061340.
- [43] S. Jafarzadeh, Z Chen, F. Bobaru (2018) Peridynamic modeling of intergranular corrosion damage, *J. Electrochem*, Vol.165, pp.C362-C374.
- [44] Z. Chen and F. Bobaru, (2015) Peridynamic modeling of pitting corrosion damage, *J Mech Phys Solids*, Vol.78, pp.352-381.
- [45] S. Rokkam, M. Gunzburger, M. Brothers, N. Phan, K. Goel (2019) A nonlocal peridynamics modeling approach for corrosion damage and crack propagation, *Theor Appl Fract Mec* Vol.101, pp.373-387.
- [46] S.A. Silling, O. Weckner, A. Askari, F. Bobaru (2010) Crack nucleation in a peridynamic solid, *Int J Fract*, Vol.162. pp.219–227.
- [47] S.A. Silling and A. Askari (2005) A meshfree method based on the peridynamic model of solid mechanics. *Comput Struct*, Vol.83, pp.1526–1535.
- [48] S.A. Silling and A. Askari (2014) Peridynamic model for fatigue cracking Tech. rep. no. SAND2014-18590. Albuquerque (NM, United States): Sandia National Laboratories (SNL-NM).
- [49] G. Zhang, Q. Le, A. Loghin, A. Subramaniyan, F. Bobaru (2016) Validation of a peridynamic model for fatigue cracking, *Eng. Fract. Mech*, Vol.162, pp.76–94.
- [50] A. Freimanis and S. Kaewunruen (2018) Peridynamic Analysis of rail squats, *Appl. Sci.* Vol.8, doi.org/10.3390/app8112299.
- [51] F. Wang, Y. Ma, Y. Guo, W. Huang (2019) Studies on quasi-static and fatigue crack propagation behaviours in friction stir welded joints using peridynamic theory, *Adv. Mater. Sci. Eng*, Vol.3, pp.1-16.
- [52] X. Ma, J. Xu, L. Liu, P. Wang, Q. Feng, J. Xu (2020) A 2D peridynamic model for fatigue crack initiation of railheads, *Int. J. Fatigue*, Vol.135, doi.org/10.1016/j.ijfatigue.2020.105536.
- [53] E. Oterkus, E. Madenci (2014) Peridynamic theory and its applications. New York, Springer.
- [54] B. Kilic, E. Madenci (2010) An adaptive dynamic relaxation method for quasi-static simulations using the peridynamic theory, *Theor. Appl. Fract. Mech*, Vol.53, pp.194-201.
- [55] C.M. Hudson (1969) Effect of stress ratio on fatigue-crack growth in 7075-T6 and 2024-T3 Aluminum-Alloy Specimens, NASA TN D-5390, 1969.